Computers and Electrical Engineering 81 (2020) 106534

Contents lists available at ScienceDirect

Computers and Electrical Engineering

journal homepage: www.elsevier.com/locate/compeleceng

Analysis of rotor slot width influence on a bearingless induction motor ☆

Qifeng Ding [a], Zebin Yang [a,*], Xiaodong Sun [b,*], Qian Zhao [a], Huimin Zhu [a]

[a] School of Electrical and Information Engineering, Jiangsu University, Zhenjiang 212013, China
[b] Automotive Engineering Research Institute, Jiangsu University, Zhenjiang 212013, Jiangsu, China

ARTICLE INFO

Article history:
Received 27 June 2019
Revised 27 November 2019
Accepted 27 November 2019
Available online 6 December 2019

Keywords:
Bearingless induction motor
Analytical method
Finite element method
Suspension performance
Load characteristics

ABSTRACT

A bearingless induction motor (BIM) is a new type of motor with non-contact rotor suspension and negligible friction loss. One major imperfection of this motor is that its performance highly depends on the rotor slot width. This paper attempts to solve this problem by using a combined analytical method and finite element analysis method (FEM). Firstly, the influence on the motor starting characteristics is revealed by analytical method and verified by finite element simulation. Secondly, using the fast Fourier transform (FFT), the effect on the radial harmonic magnetic field distribution of air gap is analyzed. Meanwhile, the impact on the motor load performance is calculated. Thirdly, the relationship among the rotor slot width, the suspension force and the unbalanced magnetic pull force is explored. Finally, the simulation and experimental results show that the BIM designed by the combined analytical method and finite element calculation can not only obtain good torque characteristics and suspension performance but also has less load loss and a better accuracy in its mathematical model. This paper provides a theoretical basis and means for further design optimization of this type of motor.

1. Introduction

Using the structure similarity between the magnetic bearing and an induction motor stator, a BIM is embedded in two sets of different pole-pair windings to destroy the symmetry of air-gap magnetic field. It has some excellent characteristics, such as no wear, no lubrication and long service life, and has broad application prospects in the special electric drive area of life sciences, aerospace and semiconductor industry [1,2].

Regarding the rotor geometry of the BIM, it is similar to that of the ordinary induction motors. Its rotation and suspension are performed by the Lorentz force and Maxwell force, respectively [3,4]. For the squirrel-cage BIM, its common rotor slot types are rectangular slot, closed slot and double-cage slot. The BIMs with different rotor types and sizes have different running performances. The saturation of magnetic density in the tooth and yoke of the rotor should be taken into account for the evaluation of motor performance. Besides, the BIM torque and suspension force are generated by the change of the air gap magnetic field. Due to the magnetic circuit changes with the rotor slot size, the distribution of the high-order air gap harmonic magnetic field will simultaneously vary. Therefore, the rotor slot has significant impact on the pulsation of the

☆ This paper is for regular issues of CAEE. Reviews processed and recommended for publication to the Editor-in-Chief by Associate Editor Dr. Raymond Choo.

* Corresponding authors.
E-mail addresses: zbyang@ujs.edu.cn (Z. Yang), xdsun@ujs.edu.cn (X. Sun).

https://doi.org/10.1016/j.compeleceng.2019.106534
0045-7906/

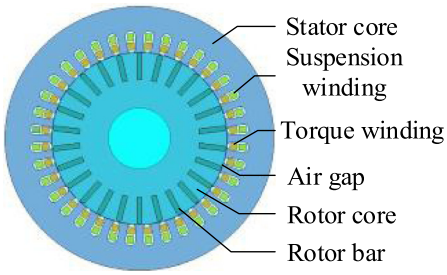

Fig. 1. Motor model structure.

BIM torque and suspension force [5,6]. In addition, the magnetic saturation is related to the rotor slot, resulting in a further influence on the BIM actual suspension force. In order to improve the starting characteristics, the rotation and suspension performance, and enhance the accuracy of the mathematical model, it is necessary to analyze and optimize the rotor slot parameters for the BIM.

In the existing methods of motor design, analytical method, finite element method and field-circuit coupling method are normally used. The analytical method takes less calculation time and the affection of the rotor parameters are directly presented [7,8]. However, it usually ignores the magnetic saturation and flux leakage phenomena. Thus, in the practical application, some correction coefficients are necessarily added to the motor mathematical model [9]. The finite element method can consider the actual factors such as flux saturation and eddy current effect, so it has high accuracy in the evaluation of motor torque, radial force and loss calculation. The field-circuit coupling method couples magnetic field with external circuit and mechanical motion. It has been used to analyze the transient performance of motor successfully and has great calculation precision.

At present, the rotor parameters have been analyzed and optimized by using those methods. In [10], a deep bar and a shallow bar were combined, and the finite element simulation shows that this structure can effectively improve the motor starting characteristics while maintaining its operating efficiency. In [11], a finite element model of the motor was used to study the influence of different rotor numbers on the bar current, output torque ripple and power factor, so as to find the reasonable stator-rotor groove ratio, making the motor a better operational performance. In [12], by deducing the analytic formula of stator and rotor current harmonics, the phenomenon was revealed that the induction motor with a closed-slot rotor does not always have lower stator current harmonics than the one with an open-slot rotor. By using open-slot structure, it effectively reduces the low-order current time harmonics. In [13], the structure of rectangular rotor slot was optimized by analytic method and the mathematical model of dynamic parameters including rotor structure size and frequency was established. This method is verified by the simulation and experiment.

The paper is organized as follows. A squirrel-cage BIM with two pole pairs is chosen. The effects of rotor slot width on torque characteristics and suspension performance are studied by field-circuit coupling method. In Section 2, the BIM model and field-circuit coupling theory are introduced. In Section 3, the motor starting characteristic is analyzed and demonstrated by simulation in *ANSYS Maxwell*. In Section 4, its load characteristic is similarly analyzed and simulated. In Section 5, the suspension performance is investigated. In Section 6, two prototypes are built, and their speed response and radial displacement are tested. In Section 7, the conclusions based on the analytical method, simulations as well as experiments are drawn.

2. The BIM model and field-circuit coupling theory

2.1. The BIM model and rotor slot parameter design

Fig. 1 shows a two-dimensional model of the motor built by *ANSYS Maxwell*. The stator adopts double-layer windings and the slot type is pyriform. The rotor has cast aluminum and the slot type is parallel. The stator and rotor core are laminated by silicon steel sheets, with a lamination coefficient of 0.98. Table 1 lists the parameters of the BIM.

Fig. 2 illustrates the distribution of torque winding and suspension winding in the stator. The pole-pair number of torque winding is 2 and the phase sequence is $+A_1$, $-C_1$, $+B_1$, $-A_1$, $+C_1$, $-B_1$. The pole-pair number of suspension winding is 1 and the phase sequence is $+A_2$, $-C_2$, $+B_2$, $-A_2$, $+C_2$, $-B_2$.

Fig. 3 shows the rotor slot structure. The initial parameters are determined as H_{s0} = =0.5 mm, H_{s2} = =1.1 mm, H_{s1} = =24.9 mm, B_{s0} = =0.6 mm, B_{s1} = =4.8 mm, and B_{s2} = =2.0 mm. The slot width B_{s0} varies from 0 to 1.8 mm. Since the slot opening area occupies a small part of the whole slot area, the variation of the rotor resistance can be ignored in the presence of slot width variation.

Table 1
The parameters of the BIM.

Parameters	Value
Stator outer diameter/mm	260
Rotor inner diameter/mm	170
Core length/mm	155
Air gap length/mm	1
Rotor outer diameter/mm	169
Rotor inner diameter/mm	60
Number of stator slots	36
Number of rotor slots	26

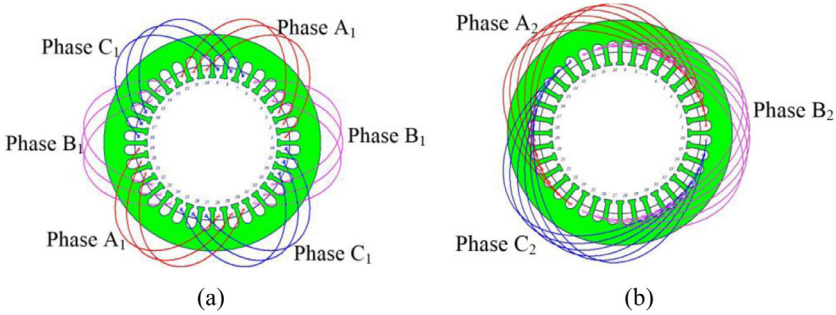

Fig. 2. Winding distribution. (a) Torque winding (b) Suspension winding.

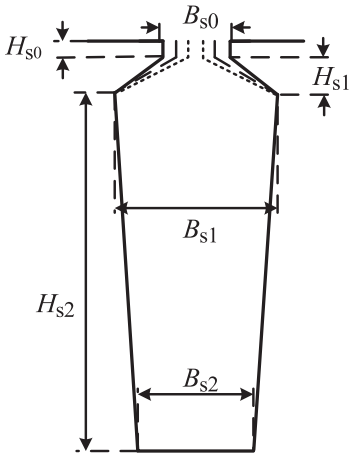

Fig. 3. Rotor slot structure.

2.2. Magnetic field model

To simplify the analysis, the following assumptions are made in the computation process of motor electromagnetic analysis.

(1) The end effect of the motor is neglected and the distribution of magnetic field along axial direction is uniform in the two-dimensional model.
(2) There is no leakage phenomenon on the outer surface of the stator and the inner surface of the rotor.
(3) The field quantities are assumed periodically varying and the temperature effect on the material is neglected.

Based on these assumptions, the 2-D transient field with magnetic vector potential A_z can be described as follows [14,15].

$$\begin{cases} \frac{\partial}{\partial x}\left(\frac{1}{\mu}\frac{\partial A_z}{\partial x}\right)+\frac{\partial}{\partial y}\left(\frac{1}{\mu}\frac{\partial A_z}{\partial y}\right)=\sigma\frac{\partial A_z}{\partial t}-J_s \\ A_z|_{\Gamma_1,\Gamma_2}=0 \end{cases} \tag{1}$$

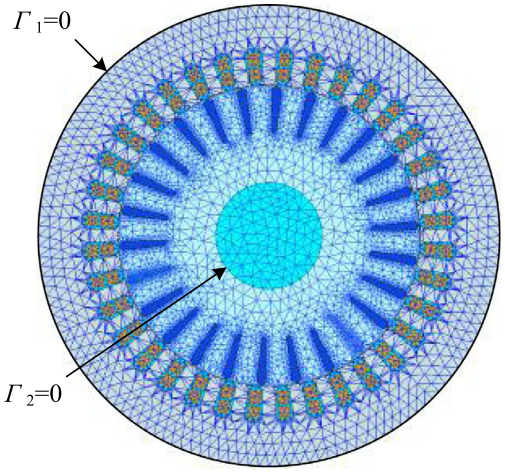

Fig. 4. Mesh generation and boundary setup of the BIM.

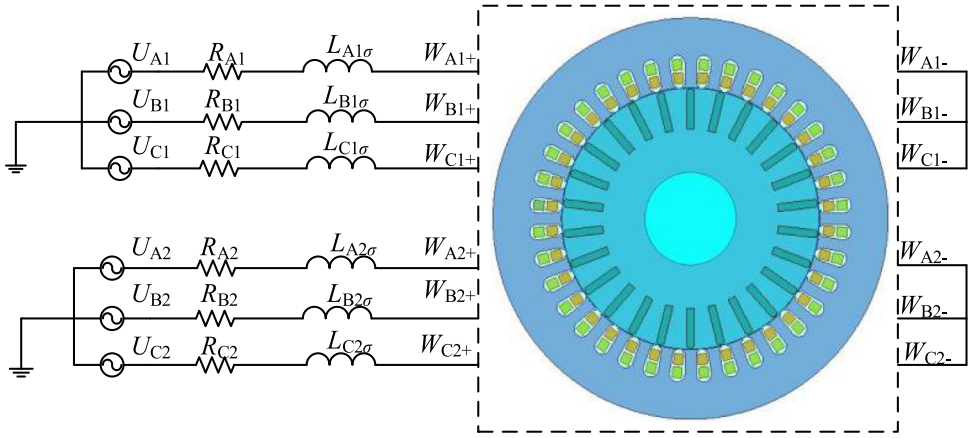

Fig. 5. Motor field-circuit coupling model.

where μ is the medium permeability, σ is the conductivity, J_s is the source current density, Γ_1 is the stator outer circumference boundary, and Γ_2 is the rotor inner circumference boundary. The mesh generation and boundary setup of the BIM is shown in Fig. 4.

Eq. (1) can be transformed into a ubiquitous equation. After the regional unit is divided and linearly interpolated, a nonlinear equation system can be obtained as

$$KA = P \tag{2}$$

where K is the coefficient matrix, A is the node magnetic vector potential, and P is the excitation. Then, by solving the equations, the vector magnetic potential of each node is gained. Finally, the electromagnetic quantities in each region of the motor can be calculated.

2.3. External circuit model

Regarding the external circuit model, the induced electromotive force of stator winding is expressed with magnetic vector and the voltage balance equation of stator winding. It has the form as

$$U_s = R_s i_s + L_\sigma \frac{di_s}{dt} + \frac{l}{S}\left(\iint_{\Omega+} \frac{\partial A_z}{\partial t} d\Omega - \iint_{\Omega-} \frac{\partial A_z}{\partial t} d\Omega\right) \tag{3}$$

where U_s and i_s are the stator phase voltage and phase current, respectively, R_s is the stator resistance, L_σ is the stator winding leakage inductance, l is the axial length of iron core, S is the stator winding cross section area, and $\Omega+$ and Ω - are the total area of the positive and negative directions of the regional phase winding coils, respectively. Fig. 5 shows the motor field-circuit coupling model.

As shown in the Fig. 5, U_{A1}, U_{B1}, U_{C1} are torque winding phase voltages, $L_{A1\sigma}$, $L_{B1\sigma}$, $L_{C1\sigma}$ are torque winding leakage inductances, W_{A1+}, W_{B1+}, W_{C1+} are torque winding beginnings, W_{A1-}, W_{B1-}, W_{C1-} are torque winding endings; U_{A2}, U_{B2}, U_{C2} are suspension winding phase voltages, $L_{A2\sigma}$, $L_{B2\sigma}$, $L_{C2\sigma}$ are suspension winding leakage inductances, W_{A2+}, W_{B2+}, W_{C2+} are suspension winding beginnings, W_{A2-}, W_{B2-}, W_{C2-} are suspension winding endings.

3. Starting characteristic analysis

The torque generation principle of the BIM is similar to the ordinary induction motors. Therefore, according to the equivalent circuit model of induction motor, the torque can be described as [16]

$$T_e = \frac{mU_{s1}^2 \frac{R'_2}{s}}{2\pi f_s\left(R_{s1}+\frac{R'_2}{s}\right)^2+\left(X_{s1\sigma}+X'_{2\sigma}\right)^2} \tag{4}$$

where T_e is the output torque, m is the number of phases, U_{s1} is the voltage of torque winding, f_s is the frequency, s is the slip, R_{s1} is the resistance of stator torque winding, $X_{1\sigma}$ is the leakage reactance of torque winding, R'_2 is the rotor resistance in stator side, and $X'_{2\sigma}$ is the rotor leakage reactance in stator side.

When $s = =1$, the starting torque T_{st} can be written as

$$T_{st} = \frac{mU_{s1}^2 R'_2}{2\pi f_s\left[(R_{s1}+R'_2)^2+(X_{s1\sigma}+X'_{2\sigma})^2\right]} \tag{5}$$

When the current frequency and the stator parameters are constant, the starting torque of the motor is determined by the equivalent leakage reactance of the rotor slot. It has been deduced that for parallel cogging, the expression of the specific flux leakage λs can be calculated as follows [17].

$$\lambda_s = \frac{H_{s0}}{B_{s0}}+2\frac{H_{s1}}{B_{s0}+B_{s1}}+c \tag{6}$$

The specific rotor slot leakage flux is composed of two parts, that is

$$\begin{cases}\lambda_U = \frac{H_{s0}}{B_{s0}} \\ \lambda_L = 2\frac{H_{s1}}{B_{s0}+B_{s1}}+c\end{cases} \tag{7}$$

where λ_U is the slot-to-drain magnetic permeability, and λ_L is the specific leakage flux of the lower part of the conductor, and c is a constant. The rotor slot width influences both λ_U and λ_L. Through the above magnetic circuit analysis method, the expression of the slot leakage reactance can be deduced as

$$X_{2\sigma} 4\pi f_r \mu l \frac{N^2}{mq}\left(\frac{H_{s0}}{B_{s0}}+2\frac{H_{s1}}{B_{s0}+B_{s1}}\right) \tag{8}$$

where f_r is the rotor current frequency, N is the number of rotor slots, and q is the number of slots per pole in each phase.

From Eqs. (5) and (8), it can be seen that the rotor leakage inductance is decreased with the increase of the rotor slot width, thus, the motor starting torque is enhanced and its loading capacity is improved.

Actually, the rotor induces not only the torque winding magnified, but also the suspension winding magnified. Therefore, the rated current of the suspension winding is usually very small compared with that of the torque winding. The rated current of the torque winding is 3A and the motor performance is compared under different suspension winding currents.

Fig. 6 illustrates the motor speed. When the suspension winding current is 5%–10% of the torque winding current, the motor operating speed is approaching its rated speed. When the suspension winding current is too large, the operating speed is apparently influenced. Thus, the rated current of the suspension winding is set as 10% of the torque winding to guarantee the normal operation of the motor.

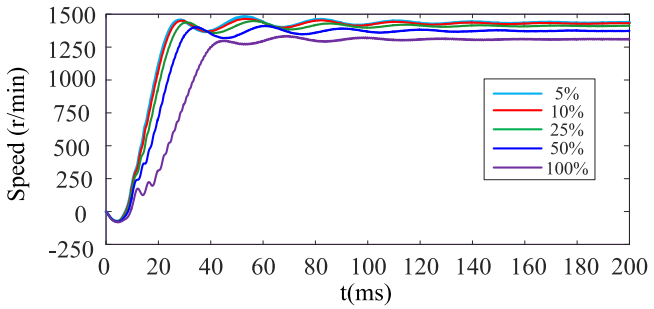

Fig. 6. Speed under different suspension winding currents.

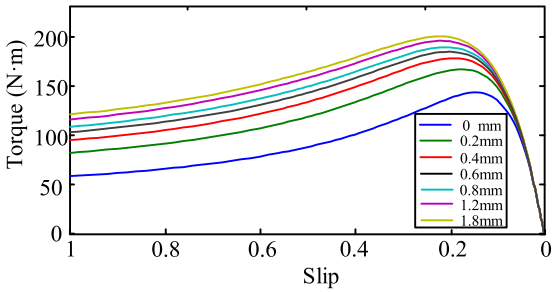

Fig. 7. Torque-slip characteristic curve.

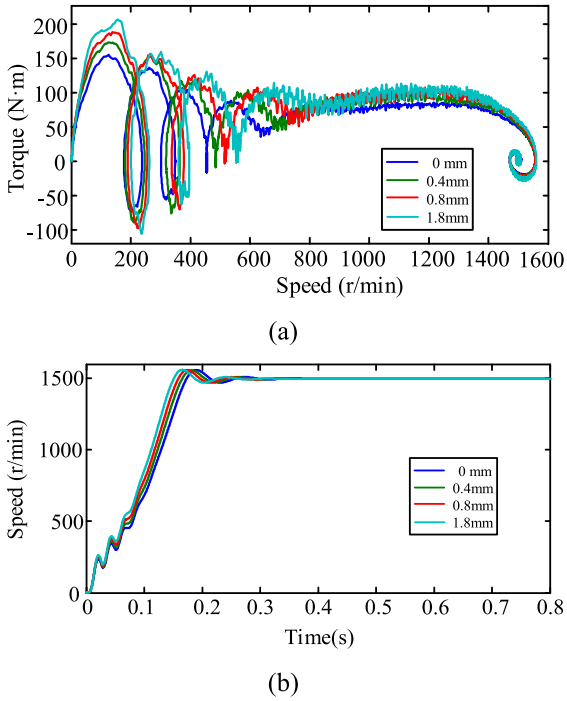

Fig. 8. Simulation results of motor starting. (a) Torque-speed curve (b) Speed response curve.

Fig. 7 shows the torque-slip curve obtained by the magnetic circuit analysis method. As shown, the starting torque and the maximum torque of the BIM are increased with the increase of the rotor slot width. When B_{s0} varies from 0 to 0.2 mm, the starting torque is increased by 41.02% and the maximum torque is increased by 16.41%, meaning that the load capacity of the closed slot rotor is weak. When B_{s0} varies from 1.2 to 1.8 mm, the starting torque is only increased by 4.58% and the maximum torque is only increased by 2.35%, which indicates that the improvement of torque characteristics is not well effective with large slot width.

Fig. 8 shows the finite element simulation results of the no-load starting performance based on field-circuit coupling method. Four motor models (B_{s0} = 0, 0.4, 0.8, and 1.8 mm) are respectively built in the simulation process. The torque winding adopts full pressure starting mode.

As shown in Fig. 8(a), the output torque is increased with the slot width, which is consistent with the conclusion of the magnetic circuit analysis. Meanwhile, it can be found that the motor torque fluctuates slightly at the beginning. Because of the sudden change in the stator winding voltage, many harmonic components are generated, leading to the large torque fluctuation. As shown in Fig. 8(b), the motor with larger slot width has a quicker response speed than that with smaller slot width. Before reaching 500r/min, the motor speed vibrates slightly due to the torque ripple.

Table 2
Motor torque ripple.

Rotor slot width/mm	Average torque/(N m)	Standard deviation of torque /(N m)	Torque ripple coefficient
0	40.10	0.89	2.22%
0.4	39.98	1.58	3.95%
0.8	40.01	1.92	4.79%
1.8	40.03	2.15	5.37%

4. Load characteristic analysis

4.1. Load torque

Load torque characteristic is one of the significant factors reflecting the motor load characteristics. Therefore, load simulation is carried out with the above four motor models. The rated load torque formula of an induction motor can be expressed by

$$T_e = \frac{9549 \times P}{n} \tag{9}$$

where T_e is the motor rated torque, P is the rated power, and n is the rated speed. Substitute $P = =10$ kW and $n = =1500$ r/min into Eq. (8), the rated load torque of the BIM is about 60 N m.

Fig. 9 shows the load torque in stable state when the load is 40 N m. It can be seen that the load torque ripple is increased with the increase of the rotor slot width, which may result in the instability.

In order to compare the effect of slot width on torque ripple directly, torque ripple coefficient is defined as the ratio of the mean torque and its standard deviation. It has the form as

$$k = \frac{\sqrt{\frac{1}{n}\sum_{i=1}^{n}(T_i - T_{avg})^2}}{T_{avg}} \times 100\% \tag{10}$$

where k is torque ripple coefficient, T_i is instantaneous torque of motor in stable state, and T_{avg} is average torque. According to the definition, the torque ripple coefficient with different slot width is calculated, as listed in Table 2.

The average torque is very close to the load torque, but the torque ripple coefficient increases with the increase of the slot width. Compared with the slot width of 1.8 mm, the torque ripple coefficient of the closed slot is reduced by 3.15%. This means that reducing the slot width of the rotor can effectively decrease the torque ripple, because the magnetic permeability of the closed groove is larger, the torque ripple can be more effectively eliminated. Similarly, when the load torque is increased to 50 and 60 N m, the motor torque ripple of the closed slot is also reduced respectively by 3.52% and 3.78%, respectively, compared with those with 1.8 mm as the open slot. It demonstrates that appropriate reduction of the width of the rotor slot can effectively suppress the motor torque fluctuation.

4.2. Magnetic field analysis

Fig. 10 shows the magnetic flux density distribution of the BIM under load state. The magnetic field distribution under different slot widths is similar. The magnetic field density in the stator yoke is relatively dense and in the rotor yoke is sparse. However, in rotor tooth, there exists partial magnetic saturation. In Fig. 10(a), as the rotor slot width is 0 mm (closed slot), the magnetic field is saturated in many parts of the rotor tooth, and the maximal flux density is 3.17 T. When the rotor slot width is 1.8 mm, the saturation only occurs in two places of rotor tooth, and one is 2.54 T, while another is 1.97 T. This indicates that the flux saturation in the rotor tooth is eased with the increase of the slot width. However, this is not applicable to the stator tooth. By comparing the magnetic density of stator tooth with different slot widths, it can be found that excessive slot width will aggravate the stator flux saturation. Besides, it can be found the greater the slot width, the greater the magnetic density of the rotor core.

Fig. 11 shows the radial distribution of the air-gap flux density along the rotor circumference. It can be found that the amplitude and distortion of air-gap flux are increased with the increase of the slot width.

To further study the distortion degree of air-gap flux, the harmonic analysis is carried out by FFT. Fig. 12 shows the main harmonic components of air-gap flux and Table 3 lists the calculation of total harmonic distortion (THD).

As shown in Fig. 12, the main harmonic orders are 12, 14, 17, 35 and 37, and the harmonic order with largest amplitude is 17, which is caused by the tooth harmonics of stator open slot. Since the magnetic field generated by the motor suspension winding and that by the torque winding are superimposed, the symmetry of the air gap magnetic field is destroyed, so there exists a large amount of even harmonics.

Table 3 shows the relationship between the air gap magnetic field distortion rate and the rotor slot width. As shown, the THD of air-gap magnetic field is increased with the increase of the rotor slot width. Therefore, choosing a smaller slot width is beneficial to reducing the air-gap flux density harmonics and decreasing the torque ripple.

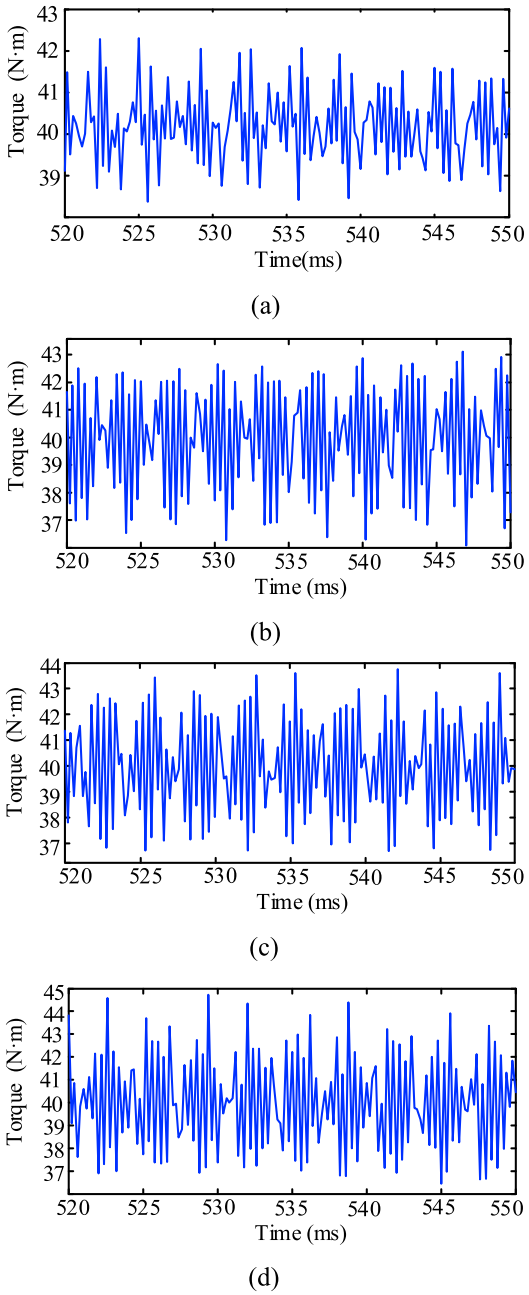

Fig. 9. Motor output torque. (a) Bs0 = =0 mm (b) Bs0 = =0.4 mm (c) Bs0 = =0.8 mm (d) Bs0 = =0.8 mm.

4.3. Load loss

Load loss mainly includes iron loss, copper loss and additional loss, where iron loss and copper loss are the majority. The iron loss includes the eddy current loss and hysteresis loss caused by alternating magnetic flux in the motor core. The formula of iron loss can be described as [18,19].

$$P_{\mathrm{Fe}} = K_h f B_m^2 + K_c f^2 B_m^2 + K_e f^{1.5} B_m^{1.5} \tag{11}$$

where P_{Fe} is the iron loss, K_h is hysteresis coefficient, f is the frequency of alternating flux, B_m is magnetic field amplitude, K_c is eddy current loss coefficient, and K_e is excess coefficient. Since the magnetic flux frequency in the rotor core is low, the rotor iron loss can be neglected.

Copper loss consists of the stator and rotor winding losses. Because the stator winding is made of multi-stranded conductor, the eddy current loss caused by skin effect can be neglected. Therefore, the calculation formula of stator copper loss can be written as

$$P_{sCu} = 3(I_{s1}^2 R_{s1} + I_{s2}^2 R_{s2}) \tag{12}$$

where I_{s1} and I_{s2} are the effective value of torque winding current and suspension winding current, respectively, R_{s2} is the resistance of stator suspension winding.

The rotor winding will produce more harmonic currents when the stator and rotor are under different speeds, leading to the uneven distribution of current density in the bars. In this case, we can use the following formula to calculate the rotor copper loss [20].

$$P_{rCu} = l \sum_{\Delta} \frac{1}{\sigma} S_{\Delta} J_{\Delta}^2 \tag{13}$$

where σ is the conductivity of the rotor guide bar, S_{Δ} is an element area in the conductor bars, and J_{Δ} is the current density in an element area. Substituting J_{Δ} into (10), the distribution of copper loss in the stator under different slot widths can be calculated, as shown in Fig. 13.

Fig. 13 shows the copper loss distribution of the stator and rotor with different slot width. It can be seen that they are both increased with the increase of the slot width. However, the increasing trend of the latter is very small. Compared with slot width of 0 mm, the copper losses of slot width of 0.8 mm and 1.8 mm are increased by 37.34% and 54.16% respectively. It will not only affect the motor efficiency, but also increase the working temperature and reduce the motor lifetime.

Fig. 14 shows the variation of stator iron loss with different slot widths. It can be seen that the stator core loss is positively correlated with the slot width. When the slot width varies from 0 to 1.8 mm, the core loss is increased by 12.55%.

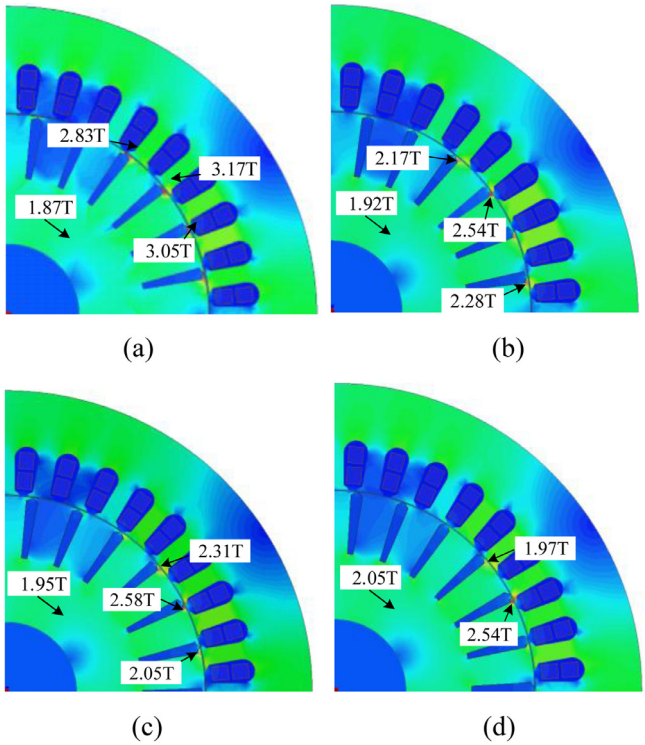

Fig. 10. Magnetic field of motor under load. (a) Bs0 = =0 mm (b) Bs0 = =0.4 mm (c) Bs0 = =0.8 mm (d) Bs0 = =1.8 mm.

Table 3
Calculation results of THD.

Slot width/mm	THD/%
0	41.66
0.4	43.90
0.8	44.11
1.8	46.83

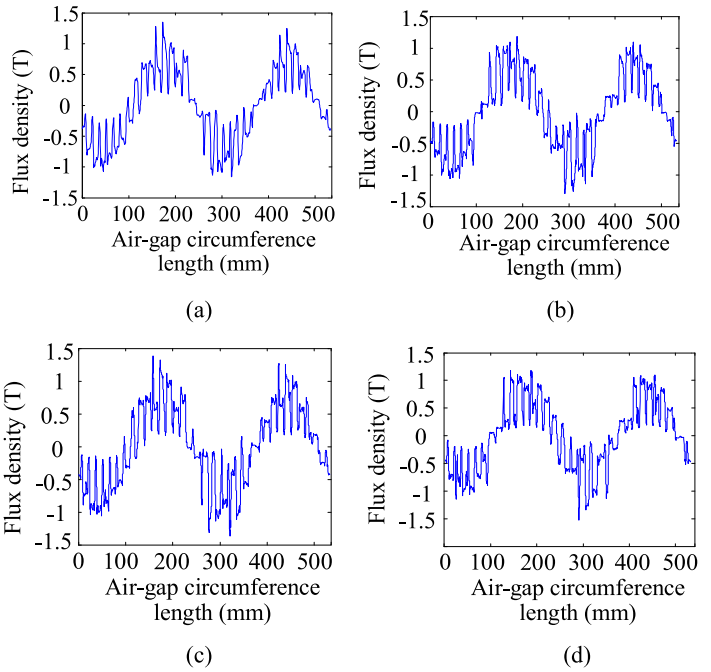

Fig. 11. Distribution of air gap radial flux density. (a) Bs0 = =0 mm (b) Bs0 = =0.4 mm (c) Bs0 = =0.8 mm (d) Bs0 = =1.8 mm.

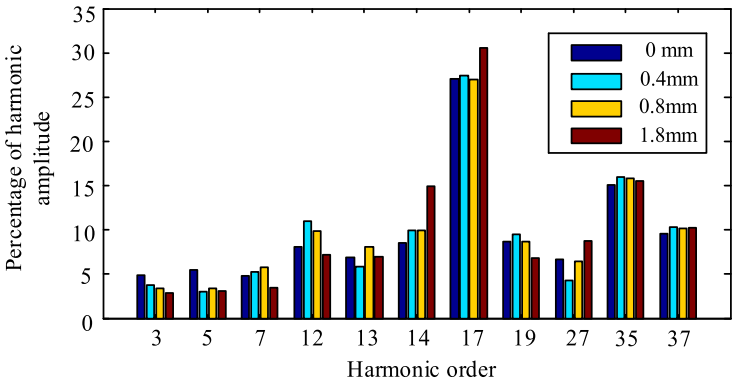

Fig. 12. Harmonic component of air-gap magnetic field.

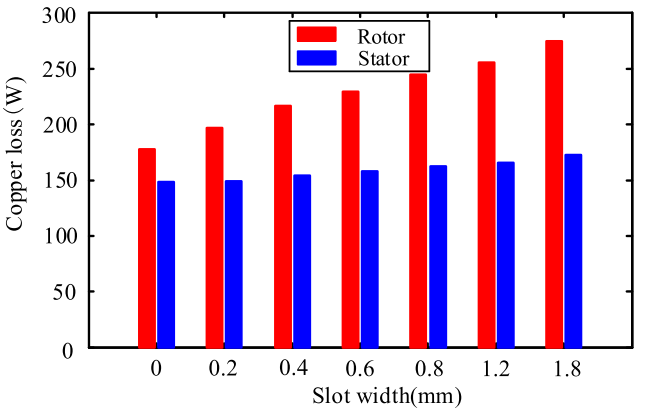

Fig. 13. Copper loss of stator and rotor.

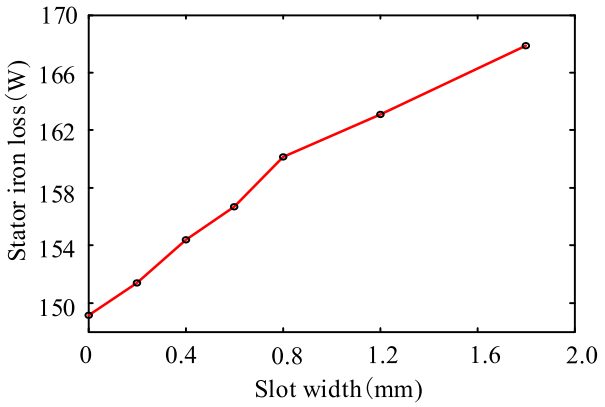

Fig. 14. Motor core loss.

Therefore, combined with the previous analysis, if the closed slot is used, the starting performance of the motor will be greatly affected. If the slot width is too large, the motor loss will increase greatly, leading to the great energy waste. Therefore, a smaller rotor slot width is suitable in terms of the torque performance.

5. Suspension performance analysis

5.1. Suspension force generation principle of the BIM

According to Maxwell stress tensor method, the force on per unit area at the junction of rotor core and air-gap can be written as [21–23]

$$F_{\mathrm{n}} = \frac{B_{\mathrm{n}}^2(\theta, t)}{2\mu_0} \tag{14}$$

where μ_0 is air permeability, and B_{n} is air-gap radial magnetic flux density. Considering the fundamental value of air-gap flux density only, the air-gap flux density generated by torque winding and suspension winding can be written as

$$\begin{cases} B_{s1}(t,\theta) = B_1(\omega t + p_1\theta + \lambda_1) \\ B_{s2}(t,\theta) = B_2(\omega t + p_2\theta + \lambda_2) \end{cases} \tag{15}$$

where B_1 and B_2 are the fundamental values of the air-gap flux density generated by torque winding and suspension winding, respectively, p_1 and p_2 are the pole-pair number of torque winding and suspension winding, respectively, λ_2 and λ_2 are the initial phase of two magnetic fields, respectively, ω is angular frequency, θ is rotor angular position. Therefore, the composed magnetic field has the form as

$$B = B_{s1}(t,\theta) + B_{s2}(t,\theta) \tag{16}$$

The radial force on the rotor core surface along the x and y directions can be expressed as

$$\begin{cases} \mathrm{d}F_{mx}(\theta) = \frac{lr^2\cos\theta \mathrm{d}\theta}{2\mu_0} \\ \mathrm{d}F_{my}(\theta) = \frac{lrB^2\sin\theta \mathrm{d}\theta}{2\mu_0} \end{cases} \tag{17}$$

where r is the rotor outer radius. By substituting (13) into (14) and integrating along the rotor surface, the radial suspension force is described as

$$\begin{cases} F_{mx} = \frac{\pi lrB_1B_2}{2\mu_0}\cos(\lambda_1 - \lambda_2) \\ F_{my} = \frac{\pi lrB_1B_2}{2\mu_0}\sin(\lambda_1 - \lambda_2) \end{cases} \tag{18}$$

From (15), it can be seen the amplitude of the magnetic field determines the value of radial force, while the phase of magnetic field determines its direction. In practice, the suspension force is controlled by changing the magnitude and phase of suspension winding current.

When the rotor is eccentric, there exists an unbalanced magnetic force. It can be expressed as [24]

$$\begin{cases} F_{\delta x} = k_\delta x \\ F_{\delta y} = k_\delta y \end{cases} \tag{19}$$

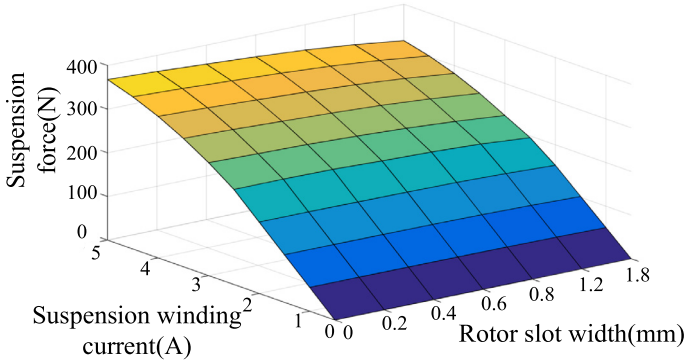

Fig. 15. Suspension force varies with suspension current.

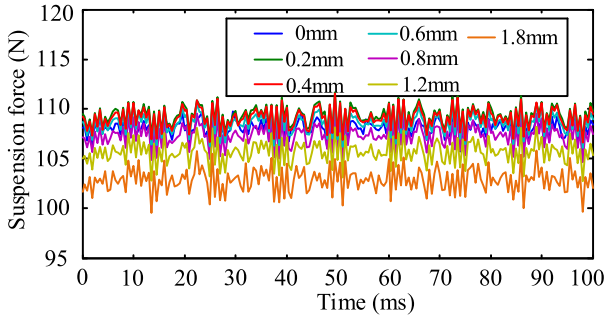

Fig. 16. Waveform of suspension force varies with time.

where $F_{\delta x}$ and $F_{\delta y}$ are the magnetic force in x direction and y direction, respectively, $k_\delta = k\frac{\pi rlB^2}{\mu_0\delta}$, k is a fading factor, δ is the air-gap length, x and y are the eccentricity distances, respectively. Therefore, the resultant force on the rotor is [25]

$$\begin{cases} F_x = F_{mx} + F_{\delta x} \\ F_y = F_{my} + F_{\delta y} \\ F_s = F_x + F_y \end{cases} \tag{20}$$

where F_s is actual force on the rotor.

5.2. Suspension force analysis

Fig. 15 shows the variation of suspension force with rotor slot width when the torque current is 3A. It can be seen that the suspension force is decreased with the increase of the slot width and is linear to the suspension winding current under the condition that the suspension current is less than the torque winding current. However, when the suspension winding current is larger than the torque winding current, the suspension force increases nonlinearly because the air-gap magnetic field has been saturated. At the same time, it can be found that the larger the rotor slot width, the more obvious the nonlinear relationship between the suspension force and the current. This is caused by the magnetic saturation analyzed in Section 3.2. The magnetic saturation occurs when the rotor slot width is large, and the excitation magnetic field no longer enhances. Therefore, if the rotor slot width is too large, the actual suspension force will deviate.

Fig. 16 shows the variation of the suspension force with time when the torque current is 3 A and the suspension current is 1 A. As shown, the suspension force is decreased as the increase of the rotor slot width.

To compare the fluctuation of suspension force, the coefficient of the suspension force ripple is defined and its expression is similar to the torque ripple coefficient. Table 4 lists the suspension force coefficient of different rotor slot widths.

As shown, when the rotor adopts a closed groove type, the suspension force pulsation coefficient is the smallest, but the average force is slightly smaller. When the open groove is used, the suspension force decreases with the increase of the slot width. The pulsation increases gradually, negatively impacting the suspension performance of the motor.

Fig. 17 shows the unbalanced magnetic force of different slot widths when the rotor eccentric distance is 0.05 mm in the x direction. It can be seen that the unbalanced magnetic force is sinusoidal approximately. The amplitude of unbalanced force is decreased with the increase of the slot width and is much smaller than the suspension force.

Fig. 18 shows the relationship between the unbalanced magnetic force and the rotor eccentric distance under different slot widths. As shown, the unbalanced force is increased with the eccentricity and decreased with the increase of the slot

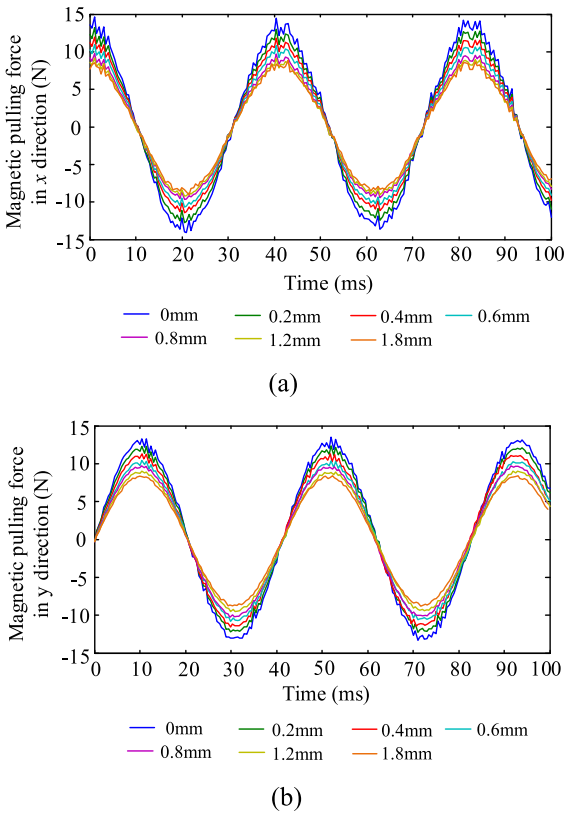

Fig. 17. Curve of unbalanced magnetic force varies with time. (a) Magnetic force in x-direction (b) Magnetic force in y-direction.

width. Therefore, for a small slot rotor, a larger suspension force can be obtained, but it has negative impact on motor controlling, for the unbalanced magnetic force is enhanced. Similarly, for a wide slot rotor, it is possible to reduce the unbalanced magnetic force but the suspension force is decreased. Thus, it is necessary to consider these two factors when designing a motor.

Through the above analysis of the torque and suspension performance, it can be seen that the slot width has the greatest impact on the motor loss, followed by starting performance. Firstly, to reduce the loss and improve the motor efficiency, a smaller slot width (less than 0.6 mm) should be chosen. Secondly, the starting performance of motor should be taken into account. When the slot width is less than 0.4 mm, the maximum output torque of motor is smaller and the load capacity is lower, so it is not adopted. Then, comparing the motor with slot width of 0.4 and 0.6 mm, it can be found that the influence of slot width on the torque ripple and suspension characteristics is small. Therefore, the slot width between 0.4 and 0.6 mm is suitable for the model proposed in this paper.

6. Experimental results and analysis

To further verify the conclusions, two prototypes with slot widths of 0.4 mm and 1.8 mm are used to compare the torque and suspension performance in terms of speed response and radial displacement. In the experiment, the other parameters of the two prototypes are the same. The two prototypes use the same structure and material of the stator. When machining

Table 4
Coefficient of the suspension force ripple.

Rotor slot width/mm	Average suspension force /(N)	Standard deviation /(N)	Suspension force ripple coefficient
0	108.02	1.00	0.93%
0.2	109.30	1.05	0.96%
0.4	109.07	1.07	0.98%
0.6	108.62	1.11	1.02%
0.8	107.38	1.13	1.05%
1.2	105.68	1.17	1.11%
1.8	102.86	1.22	1.19%

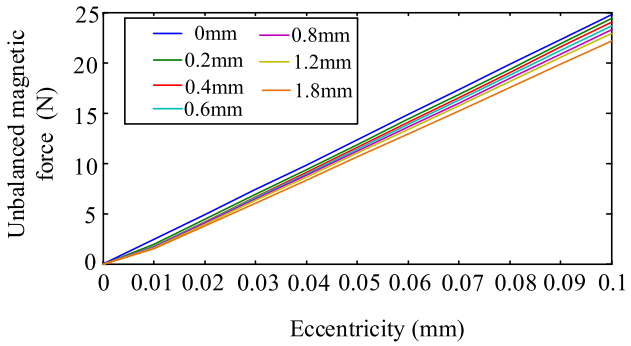

Fig. 18. Relationship between unbalanced magnetic force and eccentricity.

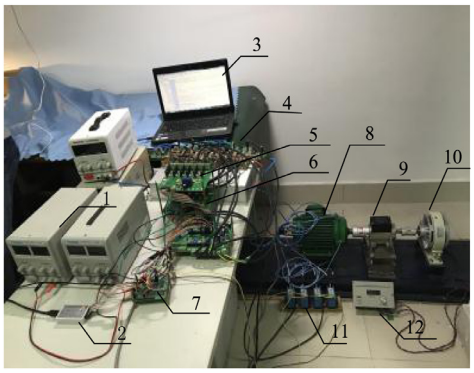

1. Power supply 2. Simulator 3. Computer 4. Inverter 5. Suspension winding module 6. Torque winding module 7. DSP main control board 8. Prototype motor 9. Torque sensor 10. Magnetic powder brake 11. Displacement sensor 12. Load regulator

Fig. 19. Prototype motor experimental platform.

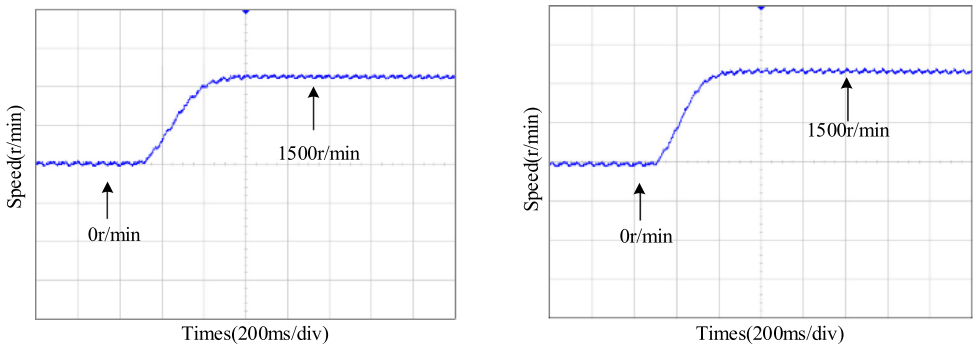

Fig. 20. Speed response. (a) Bs0 = =0.4 mm (b) Bs0 = =1.8 mm.

the rotors, only the slot width is changed. Meanwhile, the two experiments are conducted under same conditions, including the rotor and stator currents, the horizontal position as well as the measuring equipment. The prototype mainly contains four parts: suspension winding module, torque winding module, displacement sensor and torque sensor. The experimental platform is shown in Fig. 19.

Fig. 20 shows the speed response of the motor. As shown, the motor with slot width of 0.4 mm takes about 0.4 s to reach its rated speed, while the motor with slot width of 1.8 mm takes about 0.35 s. This means that the speed response of the motor is improved with the increase of slot width, but the difference is not obvious.

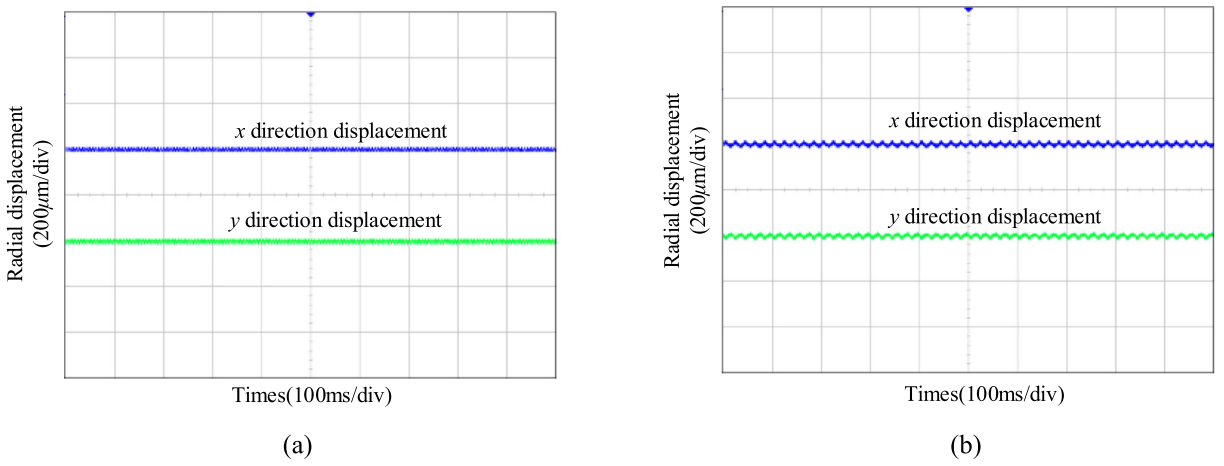

Fig. 21. Radial displacement. (a) Bs0 = =0.4 mm (b) Bs0 = =1.8 mm.

Fig. 21 illustrates the radial displacement of the rotor when the motor is operating in the stable state. As shown, the radial displacement with slot width of 0.4 mm is obviously smaller than that with slot width of 1.8 mm. The main reason for this is that when the motor is in the stable suspension state, its eccentricity is not serious, and suspension force generated by the smaller slot width is larger and the ripple is small, so the rotor radial displacement is reduced.

7. Conclusion

In this paper, the influence of rotor slot width on the performance of squirrel-cage BIM is explored by using magnetic circuit method and FEM. The rotor slot width has been optimized in terms of rotational performance and suspension performance. The following conclusions can be drawn by analyzing the starting characteristics, torque and suspension performance of the motor.

(1) The starting torque of the motor increases as the slot width increases. When selecting the closed slot, the starting torque decreases drastically. If the slot width is too large, the improvement of starting torque is not obvious.
(2) A smaller slot width can reduce the magnetic field saturation and torque ripple in the rotor teeth and effectively reduce the stator iron loss and rotor copper loss. Meanwhile, taking a smaller slot can reduce the magnetic core density of the rotor core, so that the actual value of the suspension force has a less error than the theoretical value of the mathematical model.
(3) Under the same suspension current, the suspension force decreases with slot width, so does the magnetic force. Combining the influence of slot width on the torque performance and load loss, the smaller slot width (between 0.4 mm and 0.6 mm) is a reasonable choice to make the motor achieve the best performance.

Declaration of Competing Interest

The authors declare that there is no conflict of interests regarding the publication of this paper.

CRediT authorship contribution statement

Qifeng Ding: Conceptualization, Methodology, Software, Validation. **Zebin Yang:** Data curation, Writing - original draft. **Xiaodong Sun:** Supervision. **Qian Zhao:** Visualization, Investigation.

References

[1] Sun X, Jin Z, Wang S, Yang Z, Li K, Fan Y, Chen L. Performance improvement of torque and suspension force for a novel five-phase BFSPM machine for flywheel energy storage systems. IEEE Trans Appl Supercond 2019;29(Mar (2)):0601505.
[2] Sun X, Chen L, Yang Z, Zhu H. Speed-sensorless vector control of a bearingless induction motor with artificial neural network inverse speed observer. IEEE/ASME Trans Mechatron 2013;18(Apr (4)):1357–13669.
[3] Ren Y, Chen XC, Cai YW, Zhang HJ, Xin CJ, Liu Q. Attitude-rate measurement and control integration using magnetically suspended control and sensitive gyroscopes. IEEE Trans Ind Electron 2017;65(Nov (6)):4921–32.
[4] Yang Z, Zhang D, Sun X, Ye X. Adaptive exponential sliding mode control for a bearingless induction motor based on a disturbance observer. IEEE Access 2018;6(Jun):35425–34.
[5] Xu XB, Liu JH, Chen S. Synchronous force elimination in the magnetically suspended rotor system with an adaptation to parameter variations in the amplifier model. IEEE Trans Ind Electron 2017;65(Feb (12)):9834–42.
[6] Sun X, Shi Z, Chen L, Yang ZB. Internal model control for a bearingless permanent magnet synchronous motor based on inverse system method. IEEE Trans Energy Convers 2016;31(Jul (4)):1539–48.

[7] Shi Z, Sun X, Cai Y, Yang Z, Lei G, Guo Y, Zhu J. Torque analysis and dynamic performance improvement of A PMSM for EVs by skew angle optimization. IEEE Trans Appl Supercond 2019;29(Mar (2)):0600305.
[8] Sun X, Shi Z, Lei G, Guo Y, Zhu J. Analysis, design and optimization of a permanent magnet synchronous motor for a campus patrol electric vehicle. IEEE Trans Veh Technol 2019. doi:10.1109/TVT.2019.2939794.
[9] Sun X, Su B, Wang S, Yang Z, Lei G, Zhu J, Guo Y. Performance analysis of suspension force and torque in an IBPMSM with V-shape PMs for flywheel batteries. IEEE Trans Magn 2018;54(Nov (11)):810504.
[10] Lee HJ, Im SH, Um DY, Park GS. A design of rotor bar for improving starting torque by analyzing rotor resistance and reactance in squirrel cage induction motor. IEEE Trans Magn 2018;54(Mar (3)):1–4.
[11] Gundogdu T, Zhu ZQ, Mipo JC. Influence of rotor slot number on rotor bar current waveform and performance in induction machines. Int Conf Electr Mach Syst 2017:1–6.
[12] Zhou GY, Shen JX. Current harmonics in induction machine with closed-slot rotor. IEEE Trans Ind Appl 2017;53(Jan-Feb (1)):134–42.
[13] Du XF, Hou YZ, Sun C, Zhou YJ. Optimization analysis of rectangular rotor slot of cage induction motor operating with aero variable frequency power. Chin J Aeron 2015;36(Feb (2)):614–24.
[14] Huangfu YP, Wang SH, Qiu J, Zhang HJ, Wang GL, Zhu JG. Transient performance analysis of induction motor using field-circuit coupled finite-element method. IEEE Trans Magn 2014;50(Feb (2)):873–6.
[15] Ho SL, Li HL, Fu WN. A post-assembly magnetization method of direct-start interior permanent magnet synchronous motors and its finite-element analysis of transient magnetic field. IEEE Trans Magn 2012;48(Nov (11)):3238–41.
[16] Sun X, Shi Z, Yang Z, Wang S, Su B, Chen L, Li K. Digital control system design for bearingless permanent magnet synchronous motors. Bull Pol Acad Sci 2018;66(5).
[17] Junaid Akhtar M, Behera RK, Parida SK. Optimized rotor slot shape for squirrel cage induction motor in electric propulsion application. In: IEEE India international conference on power electronics; 2014. p. 1–5.
[18] Toda H, Senda K, Morimoto S, Hiratani T. Influence of various non-oriented electrical steels on motor efficiency and iron loss in switched reluctance motor. IEEE Trans Magn 2013;49(Jul (7)):3850–3.
[19] Sun X, Shen Y, Wang S, Lei G, Yang Z, Han S. Core losses analysis of a novel 16/10 segmented rotor switched reluctance BSG motor for HEVs using nonlinear lumped parameter equivalent circuit model. IEEE/ASME Trans Mechatron Apr. 2018;23(Apr (2)):747–57.
[20] Lee JJ, Kim YK, Nam H, Ha KH, Hong JP, Hwang DH. Loss distribution of three-phase induction motor fed by pulsewidth-modulated inverter. IEEE Trans Magn 2004;40(Mar (2)):762–5.
[21] Sun X, Chen L, Yang Z. Overview of bearingless permanent-magnet synchronous motors. IEEE Trans Ind Electron 2012;60(Dec (12)):5528–38.
[22] Yang Z, Chen X, Sun X, Bao C, Lu J. Rotor radial disturbance control for a bearingless induction motor based on improved active disturbance rejection control. Int J Comput Math Electr Electron Eng 2019;38(Feb (1)):138–52.
[23] Sun X, Su B, Chen L, Yang Z, Xu X, Shi Z. Precise control of a four degree-of-freedom permanent magnet biased active magnetic bearing system in a magnetically suspended direct-driven spindle using neural network inverse scheme. Mech Syst Signal Process 2017;88:36–48.
[24] Sun X, Su B, Chen L, Yang Z, Li K. Design and analysis of interior composite-rotor bearingless permanent magnet synchronous motors with two layer permanent magnets. Bull Pol Acad Sci 2017;65(6):833–43.
[25] Yang Z, Wang K, Sun X, Ye X. Load disturbance rejection control of a bearingless induction motor based on fractional-order integral sliding mode. Proc Inst Mech Eng Part I 2018;232(10):1356–64.

Qifeng Ding was born in Sichuan Province, China in 1994. Now he is a Master Degree Candidate in Jiangsu University. His main research direction is the bearingless induction motor and its intelligent control technology.

Zebin Yang is a professor in the School of Electrical and Information Engineering, Jiangsu University. From 2014 to 2015, he was a Visiting Scholar with the School of Electrical, Mechanical, and Mechatronic Systems, University of Technology Sydney, Sydney, Australia. His main research interests include motor and its intelligent control and magnetic levitation transmission technology.

Xiaodong Sun was born in Jiangsu Province, China in 1981. Now he is a Professor with the Automotive Engineering Research Institute. His main research interests include electrical machines and drives, drives and control for electric vehicles, and intelligent control.

Qian Zhao was born in Jiangsu Province, China in 1994. Now she is a Master Degree Candidate in Jiangsu University. Her main research direction is the bearingless induction motor and its intelligent control technology.

Huimin Zhu was born in Jiangsu Province, China in 1994. Now she is a Master Degree Candidate in Jiangsu University. Her main research direction is the bearingless induction motor and its intelligent control technology.